



Single Ag atom engineered 3D-MnO₂ porous hollow microspheres for rapid photothermocatalytic inactivation of *E. coli* under solar light

Dehua Xia^{a,b}, Huadan Liu^a, Bohong Xu^a, Yunchen Wang^a, Yuhong Liao^a, Yajing Huang^a,
Liquan Ye^c, Chun He^{a,b,*}, Po Keung Wong^d, Rongliang Qiu^{a,b,*}

^a School of Environmental Science and Engineering, Sun Yat-sen University, Guangzhou, 510275, China

^b Guangdong Provincial Key Laboratory of Environmental Pollution Control and Remediation Technology, Guangzhou, 510275, China

^c Engineering Technology Research Center of Henan Province for Solar Catalysis, Collaborative Innovation Center of Water Security for Water Source Region of Mid-line of South-to-North Diversion Project of Henan Province, College of Chemistry and Pharmaceutical Engineering, Nanyang Normal University, Nanyang, 473061, China

^d School of Life Sciences, The Chinese University of Hong Kong, Shatin, NT, Hong Kong SAR, China

ARTICLE INFO

Keywords:

Atomic Ag
Water disinfection
Escherichia coli
Photothermocatalytic
Solar light

ABSTRACT

Atomic level Ag loaded MnO₂ porous hollow microspheres (Ag/MnO₂ PHMs) were prepared by redox precipitation method, and utilized for *E. coli* inactivation under solar light irradiation. Ag nanoparticles (NPs) can be downsized into single atoms, thereby realizing highly utilization of Ag element as well as achieving superior photothermocatalytic *E. coli* inactivation for Ag/MnO₂ than MnO₂ PHMs. Under attack by the optimal 0.3%Ag/MnO₂ PHMs with atomic Ag, 7.11 log₁₀ cfu/mL cells can be completely inactivated within 10 min, much faster than the 0.3%Ag/MnO₂ PHMs with Ag cluster (3.3 log₁₀ cfu/mL) prepared by photodeposition method, demonstrating the feasibility of redox precipitation to prepare efficient catalyst for water disinfection. Three effects are believed to contribute to this bacterial inactivation enhancement: (1) atomic Ag with high conductivity induces more formation of Mn³⁺ and oxygen vacancies in MnO₂, which can efficiently accelerate the separation of hot electrons and holes generated by MnO₂, collectively work with itself generated hot electrons to form into reactive species for photocatalysis; (2) atomic Ag exhibits strong local heating effect and induces higher reducibility for MnO₂, considerably enhances the photothermal conversion and lattice oxygen activity of MnO₂, thus promoting the thermocatalysis; and (3) the synergism of solar light driven photocatalysis and thermocatalysis through the activated O₂. The highly efficient photothermocatalysis make the designed 3D atomic Ag/MnO₂ PHMs have a promising antibacterial ability for cleaning the microbial contaminated water environment.

1. Introduction

Worldwide, more than half of billion people are reliant on a drinking water source contaminated with pathogenic microorganisms, such as bacteria, fungi and viruses [1]. As a result, over half a million deaths each year related to the consumption of unsafe water, with a majority of deaths caused by waterborne illnesses like cholera, typhoid, and diarrhea [2,3]. Chemical disinfection methods like chlorination and ozonation are considered as the most practical solution to provide safe drinking water, but they need to consume specific materials, and present risks to the promotion of persistent antibiotic resistance and formation of disinfection byproducts [4–6]. In contrast, photocatalytic disinfection has been considered as a sustainable and cost-effective alternative process, because of its lower cost, high efficiency, recyclable, limited disinfection byproducts, and the capability of full use of solar

energy [7–10].

Advanced photocatalysts that can effectively harness solar energy for water treatment have been extensively explored, involving modified TiO₂ and non-TiO₂ based materials, such as metal oxides, sulfides, and non-metal g-C₃N₄, red phosphorus, etc. [11–14]. As a n-type semiconductor, earth abundant MnO₂ showed widely application for pollutants elimination with attractive features such as low-cost, chemical inertness, photo-stability and nontoxicity [15]. Among these properties, its highly efficient solar driven thermocatalytic ability through the transformation between Mn⁴⁺ and Mn³⁺ and promotion of oxygen vacancies is possibly the most important [16]. In general, catalysts with different morphologies or structures exhibit different physical and chemical properties [17]. For example, MnO₂ has been synthesized into three-dimensional (3D) nanostructures such as rods, tubes, spheres and sheets, which obtained great applications in catalytic fields [18–20].

* Corresponding authors at: School of Environmental Science and Engineering, Sun Yat-sen University, Guangzhou, 510275, China.

E-mail addresses: hechun@mail.sysu.edu.cn (C. He), eesqrl@mail.sysu.edu.cn (R. Qiu).

<https://doi.org/10.1016/j.apcatb.2018.12.056>

Received 25 September 2018; Received in revised form 10 December 2018; Accepted 22 December 2018

Available online 23 December 2018

0926-3373/© 2018 Elsevier B.V. All rights reserved.

Recently, considerable attentions have been paid to the developing mesoporous materials on account of their large specific surface area, interconnected channels and abundant active sites [21]. Especially, 3D α -MnO₂ porous hollow microspheres (MnO₂ PHMs) and its modified nanocomposites have been extensively studied for catalytic ozonation [22] and anti-fouling membrane [23].

The metal oxides doped with plasmonic noble metal (Ag, Au and Pt, etc.) could achieve remarkably enhanced catalytic ability, such as Au/CeO₂, Au/MnO₂ [24,25]. The composite exhibited obvious advantages because they combine the optoelectronic properties of semiconductor with the surface plasmon resonance (SPR) effect and excellent conductivity of noble metal [26]. The SPR effect could increase its light absorption ability by scattering resonant photons and the conductivity could accelerate the separation of charge carriers [27,28]. Most importantly, the plasmonic nanometal can provide driving forces to catalytic reactions by generating hot electrons due to its photothermal effect, which will be beneficial for the photocatalysis reaction [29,30]. Some past studies have explored the use of SPR photothermal metals (e.g., Au, Ag, Cu and Al) to thermally inactivate pathogens, including photodynamic therapy and biofilm control applications [31,32]. Therefore, integrating photothermal effect into photocatalysis should be promising for utilizing the solar energy to achieve highly efficient disinfection and its mechanism has not been identified well till now [33].

Recently, single-atom catalysis has become a hot research field, because the promoted dispersion of noble metal via downsizing a nanoparticle to the atomic level can maximum enhance its utilization [34,35]. However, the modification of catalysts with atomic noble-metal remains a tough task, because the noble-metal nanoparticles with high surface energy easily agglomerate into large particles through conventional co-precipitation or photo-deposition [36–38]. Inspired by the strategy for stabilizing single-atom Au on the surface of MnO₂ rods via defect trapping by Chen et al. [39], a modified redox precipitation was developed to fabricate single-atom Ag-deposited 3D α -MnO₂ PHMs in the present study. With this preparation method, the as-prepared Ag/MnO₂ PHMs with the amount of Ag loading reduced to only 0.3% can efficiently use full solar spectrum, visible-infrared, and up to infrared light for *E. coli* inactivation. The broad-spectrum solar light utilization by Ag nanoparticle is related to the highly dispersed single-atom Ag as evidenced by Cs-corrected HAADF-STEM and EDS mapping. The synergistic inactivation by photocatalysis and thermocatalysis was substantiated and would be more desirable than photocatalysis alone for engineering practice.

2. Experimental

2.1. Materials

All chemicals used in this work are analytical grade and used without any further purification. Silver nitrate (AgNO₃) and Mn(CH₃COO)₂·4H₂O were purchased from Tianjing Yongda Chemical Reagent Co. Ltd, Na₂CO₃ were purchased from Shantou Xilong Chemical factory, KMnO₄ were purchased from Tianjing Fuchen Chemical Reagent Co. Ltd., and HCl (37%) were purchased from Guangzhou Reagent Chemical factory, respectively. In addition, the doubly-distilled deionized water was used throughout this study.

2.2. Preparation of Ag/MnO₂ porous hollow microspheres (PHMs)

MnO₂ PHMs: MnCO₃ precursor was prepared by mixing the Mn(CH₃COO)₂·4H₂O and Na₂CO₃ solutions, then MnO₂ microspheres were formed. After that, HCl (10 mM) was added to remove the MnCO₃ core, and then calcined at 400 °C for 4 h to obtain 3D MnO₂ PHMs [22,23].

Ag/MnO₂ PHMs: The preparation step was described in Scheme 1. MnO₂ PHMs was ultrasonically re-dispersed in deionized water, and then AgNO₃ solution was added. The concentrated H₂O₂ (0.5 g, 30 wt.

%) was dropwise added to the mixture of MnO₂ PHMs and AgNO₃. During the addition of H₂O₂, O₂ was emitted. $\text{MnO}_2 + \text{H}_2\text{O}_2 + 2\text{H}^+ = \text{Mn}^{2+} + 2\text{H}_2\text{O} + \text{O}_2$, where the consumption of released H⁺ can drive the hydrolysis of AgNO₃ to Ag(OH) as equation: $\text{AgNO}_3 + \text{H}_2\text{O} = \text{Ag(OH)} + \text{HNO}_3$. Because these two reactions occur simultaneously, the Ag species could be trapped by an *in situ* generated hole without aggregation. Moreover, Ag(OH) could be further reduced into metallic Ag by H₂O₂: $\text{O}_2 + 2\text{H}^+ + 2\text{e}^- = \text{H}_2\text{O}_2$ and $\text{Ag(OH)} + \text{H}^+ + \text{e}^- = \text{Ag} + \text{H}_2\text{O}$. After the redox precipitation, the solid was filtered, washed, and frozen-dried. Other Ag/MnO₂ PHMs with different deposited amount were synthesized and denoted as (x) Ag/MnO₂, x represents Ag/MnO₂ with different silver contents in preparation, which were 0.1, 0.3, and 0.5 wt. %, respectively. The accurate deposited Ag amounts for the as-prepared samples were quantified by ICP-MS. Moreover, the PD-Ag/MnO₂ PHMs prepared by photo-deposition method was also mentioned in the Text S1.

2.3. Characterizations

The X-ray diffraction (XRD) patterns of samples were recorded on a Rigaku D/max 2200 PC diffractometer with Cu K α radiation. UV–vis–NIR adsorption curve of catalysts were obtained using a UV–vis–NIR spectrophotometer (Lambda 950) with an integral-sphere attachment range from 200 to 1100 nm. XPS spectra of samples were collected on ESCALAB 250, Thermo Fisher Scientific, and USA. The morphology of samples was investigated by Quanta 400 F thermal field emission scanning electron microscopy (SEM, Shimadzu, Japan) using an acceleration voltage of 15 kV, and TEM (JEM-2010HR). The specific surface area for samples was carried out by an ASAP2010 physical and chemical adsorption instrument (USA). In addition, the photoelectrochemical performance was measured in a three electrode quartz cells system including a saturated calomel electrode (SCE) as reference electrode, platinum plate as counter electrode, and stainless steel coated with MnO₂ and Ag/MnO₂ PHMs as the working electrode with 1 M Na₂SO₄ as electrolyte.

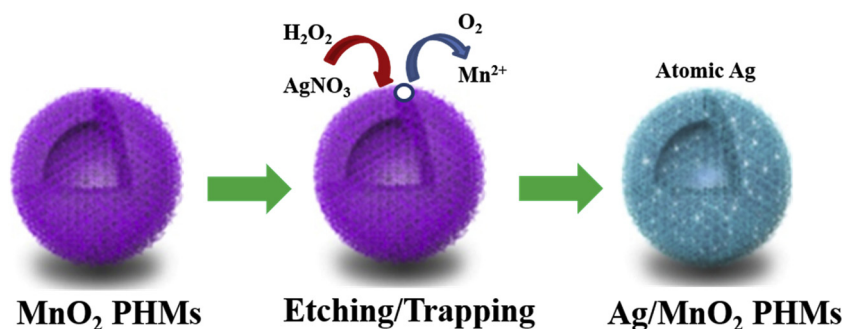
2.4. Photothermocatalytic, photocatalytic and thermocatalytic disinfection

The bacteria were cultured in nutrient broth (NB) at 37 °C for 16 h to yield a cell density of 10⁹ cfu/mL. Before test, the bacterial cells were washed twice by ultrapure water and then centrifugation (10,000 rpm for 1 min), and then diluted to 10⁷ cfu/mL. During each test, 10 mg of catalyst and 0.1 mL of bacteria solution (10⁷ cfu/mL) were added into a 50 mL beaker, then the light source was turned on (a 300 W Xenon). During each time interval, the collected sample was quickly spread on the agar plate and counted after 24 h incubation at 37 °C.

Moreover, a long-wave pass cutoff filter of 420, 480, 560, 690, or 830 nm was used individually to analyze the photothermocatalytic activity of the Ag/MnO₂ PHMs under the visible-infrared or infrared irradiation from the Xenon lamp. The light intensity of the irradiation with $\lambda > 420, 480, 560, 690, \text{ and } 830 \text{ nm}$ is 291.9, 273.3, 255.0, and 238.7, 206.2 mW/cm², respectively. To identify the photocatalytic activity of Ag/MnO₂ PHMs for *E. coli* inactivation, the reactor was placed in a water bath to maintain the ambient temperature under the irradiation of the Xenon lamp to eliminate the effect of thermal catalysis. To measure the thermocatalytic activity of the Ag/MnO₂ PHMs for *E. coli* inactivation, the reactor was placed in a water bath to maintain the temperature in the dark to eliminate the effect of photocatalysis.

2.5. Microscopic observations of bacteria

(1) SEM: after interacting with particles for 0 min, 60 min and 120 min, the cells were collected by centrifuged at 5000 rpm for 5 min, then 5 mL glutaraldehyde (2.5%) was added into the mixture to fix the cells overnight and washed twice with phosphate buffer saline (PBS) buffer, and then sequentially dehydrated with 30%, 50%, 70% and 90%



Scheme 1. Synthetic route of atomic Ag-doped MnO₂ PHMs.

ethanol for 10 min, and 100% ethanol for 20 min twice, respectively. Then specimen were lyophilized, gold sputter-coated to observe any changes in their morphologies on SEM; (2) Fluorescent-based cell live/dead test: all the bacterial samples (10^7 cfu/mL cells, 0.01 g/L catalysts) were stained with PI (propidium iodide) and SYTO9 of the Live/Dead BacLight Bacterial Viability kit, and then observed with a laser scanning fluorescence microscopy (Olympus, FV1000) [40].

2.6. Enzyme activity & Biomolecule oxidation assay

(1) The ATP synthesis ability of the treated cells at 5, 10, 20 and 30 min was monitored with the ATP assay kit, quantified by measuring absorbance at 630 nm; (2) Glutathione (GSH) was extracted using GSH-PX Assay Kit (Colorimetric method), then quantified by measuring absorbance at 630 nm. Samples were collected at 5, 10, 20 and 30 min; (3) Chromosomal DNA was extracted using an Ezup Column Bacteria Genomic DNA Purification Kit, then verified by DNA agarose gel electrophoresis (0.6% agarose gel at 100 V for 40 min in $1 \times$ TAE buffer) [41].

2.7. Photothermal effect measurement

To examine the photothermal effect induced by light irradiation, 25 mL of 1 mg/mL MnO₂ or Ag/MnO₂ PHMs dispersions were irradiated for 30 min by a Xenon lamp or NIR laser (0.5 W cm^{-2}), respectively. The temperature changes of the solutions were monitored using a submerged thermocouple microprobe. Thermo images were also taken by a thermos imager (Testo Co., Ltd., Testo 885) to perform quantitative analyses of photothermal effect of samples. A testo IR soft was used to obtain the average temperature distribution for every thermos image. The parameters of NIR laser (Laserwave, Beijing, LWIRL808-5W-F) include wavelength: 808 nm; power: 5 W; power density 0.5 W cm^{-2} ; the spot area is 50 mm^2 and the diameter is 8 mm.

3. Results and discussion

3.1. Structural analysis of the catalysts

In this strategy (Scheme 1), H₂O₂ etches the surface of α -MnO₂ PHMs through consuming released H⁺, thereby driving hydrolysis of AgNO₃ into Ag (OH), which could be then reduced into atomic Ag and subsequently trapped into surface defects of α -MnO₂ to form atomic Ag/MnO₂ PHMs. First, the wide-angle XRD patterns of as-prepared catalysts were displayed in Fig. 1a. For all samples, the distinct diffraction peaks at $2\theta = 12.7^\circ, 18.1^\circ, 28.8^\circ, 37.5^\circ, 42.1^\circ, 49.9^\circ, 56.2^\circ$, and 60.3° can be well indexed to the tetragonal α -MnO₂ phase (JCPDS 44-0141). In contrast to pure MnO₂ PHMs, the peak intensity of Ag/MnO₂ PHMs become slightly weaker but no additional peaks belonged to the crystal Ag can be found, presumably owing to the ultrafine-sized and high dispersion of nano-sized Ag [42]. Moreover, the BET surface areas decrease from $124.13 \text{ m}^2 \text{ g}^{-1}$ for MnO₂ PHMs to $104.11 \text{ m}^2 \text{ g}^{-1}$ for

0.3%Ag/MnO₂ PHMs (Table 1), confirming that Ag nanoparticles are highly dispersed and even partially filled into the porous MnO₂ PHMs. The high specific surface area and mesoporous structure of Ag/MnO₂ PHMs were conducive to the absorption and diffusion of reactants, which has a positive correlation with the amount of surface active sites [22,23]. Through the ICP-MS measurement, the loading amount of Ag in the 0.3%Ag/MnO₂ PHMs sample was determined to be 0.257 wt. % (Table 2).

The high-resolution XPS test was used to investigate the surface composition and chemical state of elements in the as-prepared catalysts. As shown in Fig. 1b, the Mn 2p_{3/2} region was resolved into three individual sub-bands, represents Mn²⁺ (640.6 eV), Mn³⁺ (641.6 eV) and Mn⁴⁺ (642.8 eV), respectively [43]. Table 2 indicates the surface concentration of Mn²⁺ + Mn³⁺ in 0.3%Ag/MnO₂ (1.06) is higher than that of MnO₂ (0.96), suggesting Ag doping can reduce Mn⁴⁺ in MnO₂. In general, the increase of low valent Mn can induce the formation of crystalline defects and oxygen vacancies in MnO₂, which are beneficial for the photocatalysis/thermocatalysis through capturing more electrons and activating reactive species [44]. Moreover, all the O 1s XPS spectra in Fig. 1c have three peaks at 529.7, 531.1 and 532.1 eV, assigned to lattice oxygen (O_L), adsorbed oxygen (O_{ads}, such as O₂⁻, O⁻ and OH group) and limited surface oxygen (H₂O), respectively [45]. Table 2 displays that molar ratio of O_L : O_{ads} in 0.3% Ag/MnO₂ PHMs (2.12) is higher than that of MnO₂ (1.78), evidencing the Ag doping can increase the formation of O_L. Generally, O_L with high mobility is favorable for the formation of reactive oxygen species through the transformation by oxygen vacancy [46]. Yang et al. also indicated that O_L can be activated by solar light irradiation, which plays a crucial role in the thermocatalytic oxidation [47]. Additionally, there are two peaks belonging to Ag-3d_{5/2} (368 eV) and Ag-3d_{3/2} (374 eV) orbital, which can be further separated and fitted into Ag⁺ and Ag⁰ species, respectively (Fig. 1d). This confirms the successful doping of Ag nanoparticles on MnO₂ PHMs.

To inspect the defined structure of 0.3%Ag/MnO₂ porous hollow microspheres (PHMs) prepared by redox-precipitation method, SEM, HRTEM, HAADF-STEM, and EDS-mapping were utilized. The SEM images in Fig. 2a show that the 0.3%Ag/MnO₂ has regular 3D porous spherical shape, and the cavity of the broken MnO₂ confirms its hollow structure. Similarly, the TEM in Fig. 2b also confirms the 3D hollow structure of 0.3%Ag/MnO₂ PHMs. As displayed in Fig. 2c, the HRTEM analysis of the 0.3%Ag/MnO₂ PHMs reveals that the polycrystalline walls of MnO₂ are grown along the [110], [310] and [211] directions, but it is hard to find Ag nanoparticles within catalyst. Interestingly, due to the difference in element contrast between Ag and Mn, the Ag species look brighter than the Mn in the dark field of Cs corrected HAADF-STEM (inset of Fig. 2c). It is found that Ag atoms (marked by white squares) obviously appearing at the edge of the MnO₂ PHMs, evidencing that the method of redox precipitation can downsize Ag nanoparticles into single atoms. The HAADF-STEM image of 0.3%Ag/MnO₂ PHMs at larger scale in Fig. 2d shows no aggregation of the Ag species. The mapping images of Ag, Mn, and O shown in Fig. 2e–h further

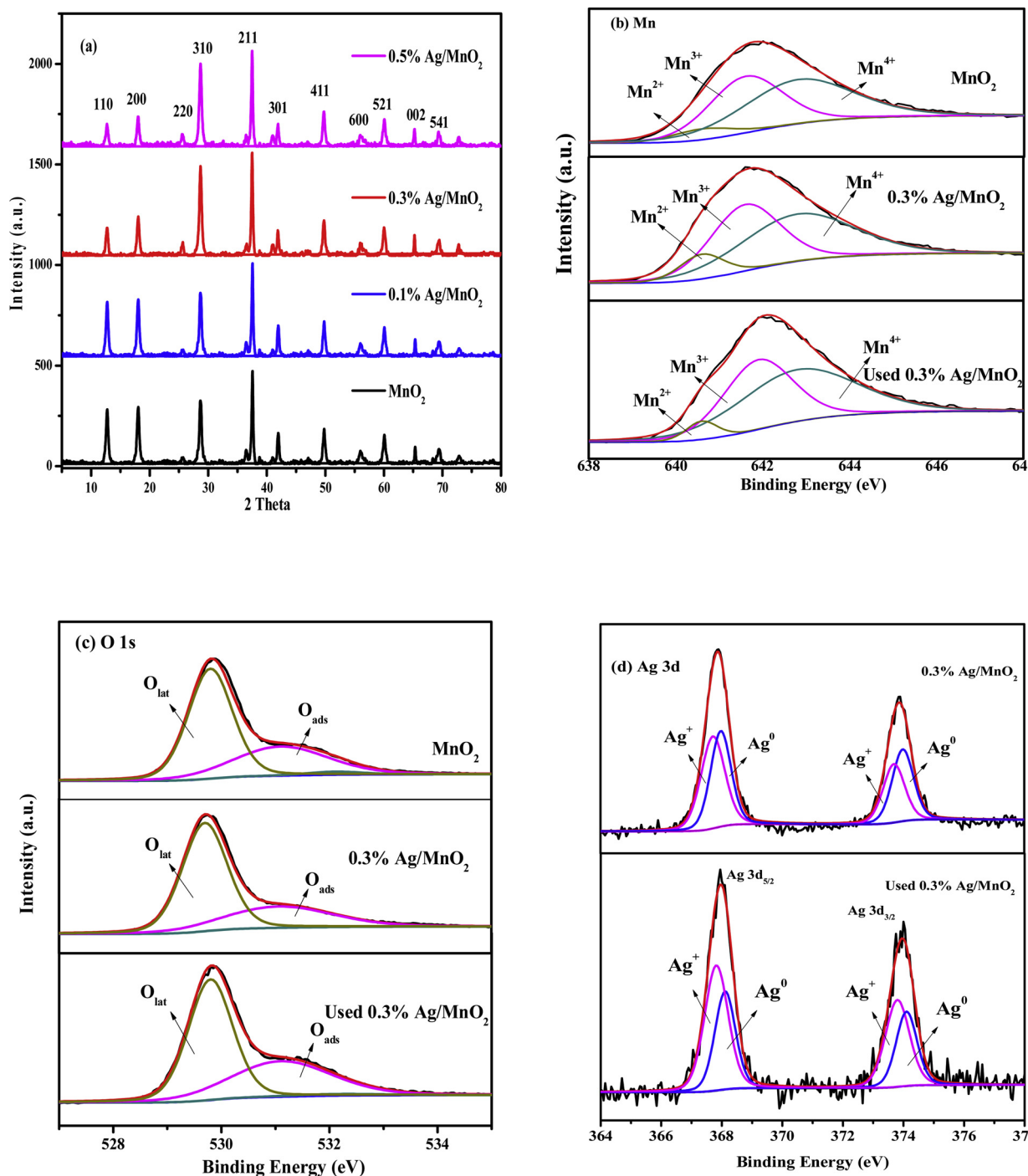


Fig. 1. (a) XRD patterns, XPS spectra of (b) Mn 2p, (c) O 1s, and (d) Ag 3d in MnO₂ and Ag/MnO₂ PHMs.

Table 1

Ag amount and specific surface area of MnO₂ and Ag/MnO₂ PHMs.

Catalysts	Ag content wt. %	S _{BET} m ² g ⁻¹
MnO ₂	0	124.13
0.1%Ag/MnO ₂	0.104	120.87
0.3%Ag/MnO ₂	0.257	104.11
0.5%Ag/MnO ₂	0.492	102.95

indicate that atomic Ag nanoparticles are homogeneously dispersed on the MnO₂ PHMs. In contrast, the great rough dots of agglomerated Ag clusters appeared on the surface of PD-0.3%Ag/MnO₂ PHMs are

evidenced by the SEM and the mapping images (Fig. S1). This further confirms the redox-precipitation method is more efficient to achieve high dispersion of Ag atoms on MnO₂ than photo-deposition method.

Raman test was utilized to further identify the effect of Ag modification on MnO₂ PHMs. As shown in Fig. 3a, both Ag/MnO₂ and MnO₂ PHMs showed two main Raman adsorption peaks. The strong peak around 305 cm⁻¹ could be attributed to the stretching vibration ν_3 (Mn-O, F_{2g} mode) in the basal plane of [MnO₆] sheets and it was considered as the symmetric stretching mode of oxygen atoms around Mn ions, while the peak around 633 cm⁻¹ (D mode) was related to oxygen vacancies due to the presence of Mn³⁺ in the MnO₂ lattice [48]. The peak fitting of the F_{2g} and D modes in the Raman spectra of both samples were conducted to calculate the ratio (I_D/I_{F2g}), which was linked to the

Table 2
Physical parameters, chemical and surface compositions of MnO₂ and Ag/MnO₂ PHMs.

Sample	Mn ²⁺ (%)	Mn ³⁺ (%)	Mn ⁴⁺ (%)	O _L (%)	O _{ads} (%)	O _{surf} (%)	Ag ⁺ (%)	Ag ⁰ (%)	Surface element molar ratio		
									Mn ²⁺	Mn ³⁺ /Mn ⁴⁺	Ag ⁰ /Ag ⁺
MnO ₂	6.79	42.13	51.09	62.21	35.23	2.16			0.96		1.78
0.3%Ag/MnO ₂	9.96	41.68	48.36	67.94	32.06	0.00	46.75	53.25	1.06		0.88
0.3%Ag/MnO ₂ (used)	6.66	42.07	51.27	63.29	35.37	1.33	39.71	60.29	0.95		0.66

oxygen defect sites of the catalysts [49]. The I_D/I_G value of pure MnO₂ PHMs and 0.3%Ag/MnO₂ PHMs was 1.75% and 4.89%, respectively. This result suggests the Ag doping induced more intrinsic defects sites and oxygen vacancies in the MnO₂ PHMs, consistent with XPS analysis.

H₂-TPR measurements were carried out to explore the reducibility of Ag/MnO₂ PHMs, because high reducibility of catalyst could favor the photothermocatalytic reaction [50]. As shown in Fig. 3b, with the increase of reduction temperature, the sample will undergo the successive reduction of surface adsorbed oxygen species, and the process of MnO₂ → Mn₂O₃ → Mn₃O₄ → MnO, respectively [51]. In contrast, the Ag/MnO₂ PHMs has stronger low-temperature reducibility than MnO₂ PHMs, as the temperatures of MnO₂ peaks decrease from 200 °C, 307 °C and 492 °C to 114 °C, 154 °C, and 250 °C, respectively. Peer references indicate that activated hydrogen on the Ag surface can easily migrate to the surface of the MnO₂ PHMs and thus facilitate the reduction reaction at low temperatures [52]. Meanwhile, the incorporated Ag also can activate surface O_L species of MnO₂ PHMs, which are easier to be desorbed and react with H₂ at low temperature [18,20]. Accordingly, the better reducibility and higher oxygen mobility for 0.3% Ag/MnO₂ cause more oxygen to be adsorbed and further excited to reactive oxygen species, which would then be involved in the photothermocatalytic reaction of Ag/MnO₂ PHMs.

To further explore the optical performance of the catalysts, the UV-vis-NIR diffuse reflectance (DRS) tests were performed (Fig. 3d). For pure MnO₂ PHMs, a light absorption in the visible light region with the absorption edge at about 650 nm corresponds to the wide bandgap of MnO₂, and a limited light absorption in the range of 800–1600 nm is attributed to the multiple scattering absorption of MnO₂ porous

structure. In contrast, Ag/MnO₂ PHMs displays an enhanced visible light (400 < λ < 800 nm) absorption resulted from the adsorption band of Ag and stronger infrared adsorption (980 < λ < 1600 nm) attributed to the plasmonic scattering effects of Ag nanoparticles [28].

3.2. Solar light-driven photothermocatalytic bacterial inactivation

The photothermocatalytic disinfection for all the as-prepared catalysts was tested under Xenon lamp. As shown in Fig. 4a, MnO₂ and 0.3%Ag/MnO₂ PHMs exhibit about 0.1–0.5 log of inactivated *E. coli* cells in the dark, indicating the catalysts have limited cytotoxicity to *E. coli*. Upon 10 min Xenon lamp irradiation (309.2 mW cm⁻²), a 0.1% Ag/MnO₂ PHMs with rare Ag content can realize 3 log of *E. coli* inactivation, but MnO₂ PHMs exhibited only about 1.12 log cell reduction within same time period, indicative of enhanced catalytic effect from Ag doping. Moreover, the Ag content on MnO₂ and preparation method exhibit great influence on the inactivation of cells. The optimal 0.5% Ag/MnO₂ PHMs can totally inactivate 7.11 log of *E. coli* within 10 min, while the 0.3%Ag/MnO₂ PHMs with lower Ag doping also obtained the similar inactivation kinetics, suggesting the highly utilization of Ag nanoparticles for 0.3%Ag/MnO₂ PHMs. When the loaded Ag increases from 0.1% to 0.3%, the inactivation efficiency can be enhanced significantly, mainly due to the high dispersion and utilization of atomic Ag. However, when the loading amounts of Ag further increased to 0.5%, the atomic Ag nanoparticles may agglomerate into large particles due to its high surface energy [42,43], thus showing limited enhancement in the *E. coli* inactivation than the 0.3% Ag loaded sample. Especially, although containing the same content of Ag, the 0.3%Ag/

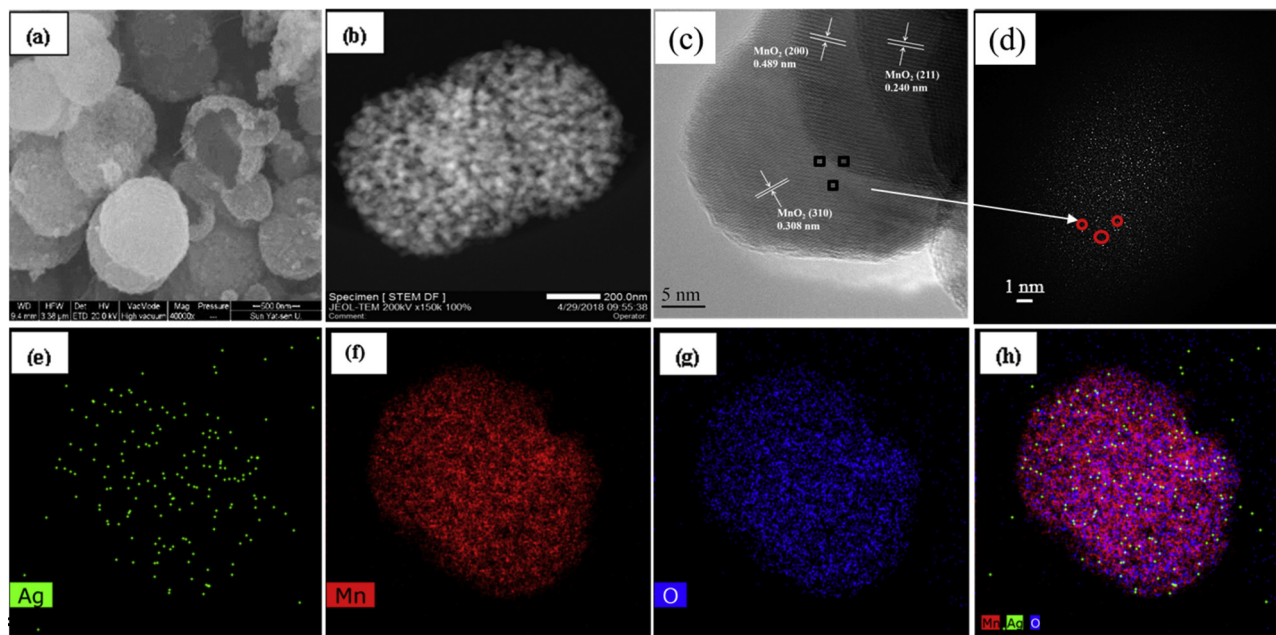


Fig. 2. (a) SEM images of 0.3%Ag/MnO₂ PHMs, (b) TEM and (c) HRTEM images of 0.3%Ag/MnO₂ PHMs, (d) Cs-corrected HAADF-STEM images of 0.3%Ag/MnO₂ PHMs at the same district with inserted partially magnified pictures, (e–h) HAADF-STEM of 0.3%Ag/MnO₂ PHMs with element distribution images corresponding to Ag, Mn, O.

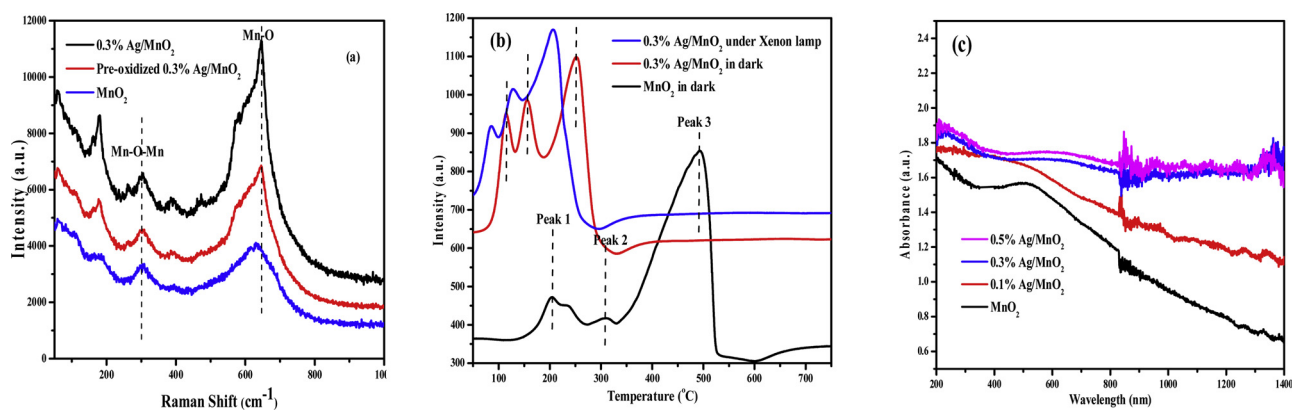


Fig. 3. (a) Raman patterns, (b) H₂-TPR profiles and (c) UV-vis-NIR adsorption curves of MnO₂ PHMs and 0.3%Ag/MnO₂ PHMs.

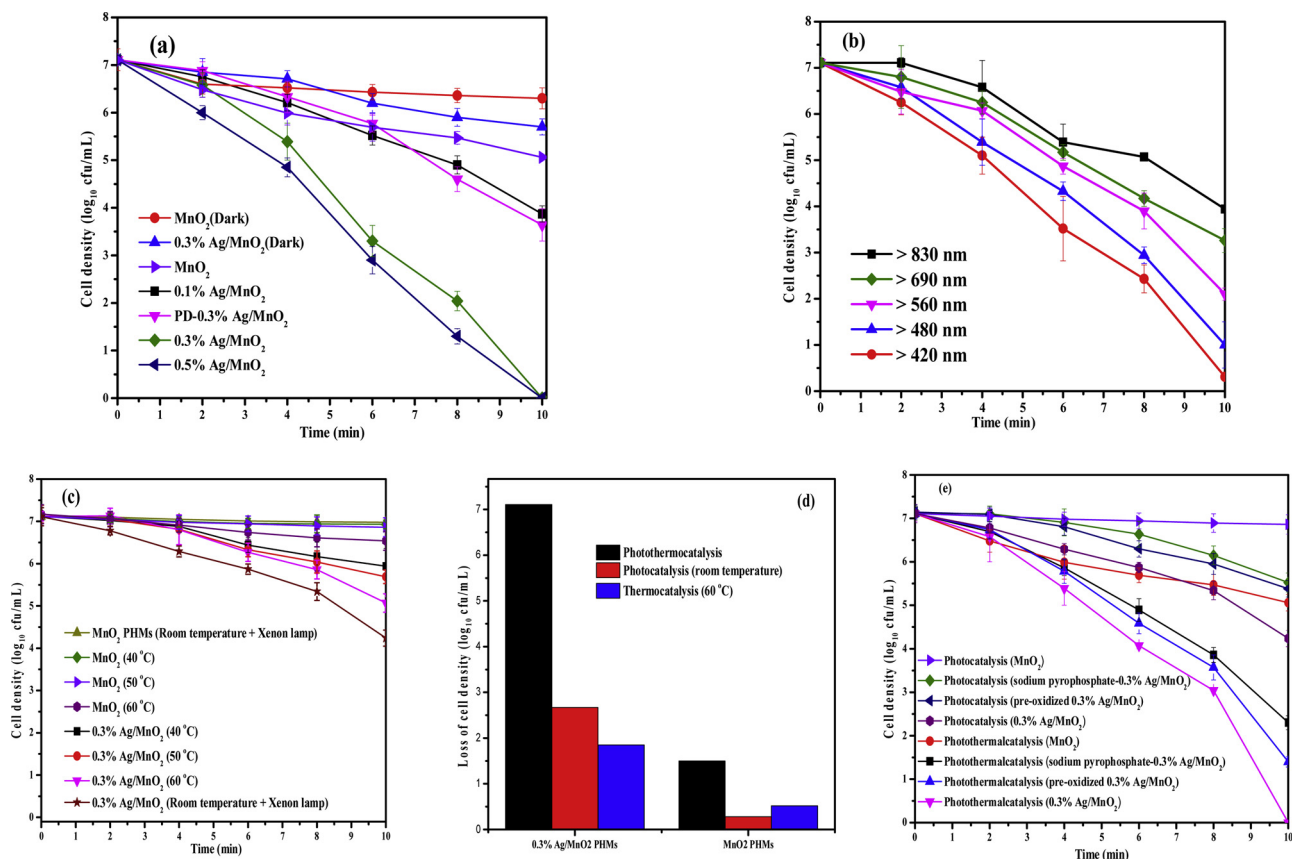


Fig. 4. Inactivation efficiency against *E. coli* (10⁷ cfu/mL) with catalysts, (a) Under Xenon lamp irradiation; (b) with different filter (420, 480, 560, 690 and 830 nm); (c) at room temperature under Xenon lamp, and at different temperature in the dark; (d) Comparison of inactivation efficiency of photothermocatalysis, photocatalysis and thermocatalysis; (e) Inactivation efficiency against *E. coli* by 0.3%Ag/MnO₂ PHMs (role of Mn³⁺ and oxygen vacancy).

MnO₂ PHMs shows a better activity than PD-0.3%Ag/MnO₂ PHMs prepared via photo-deposition (PD), demonstrating the feasibility of redox precipitation to prepare efficient catalyst for water disinfection.

The reaction proceeds through visible-infrared or infrared light with 0.3%Ag/MnO₂ PHMs was also performed under the irradiation of Xenon lamp by using different long wave pass cutoff filters. As shown in Fig. 4b, under the irradiation of visible-infrared light with the wavelength above 420, 480, 560, and 690 nm (the corresponding light intensity is 291.9, 273.3, 255.0, and 238.7 mW/cm², respectively), the corresponding survived cell density of 0.3%Ag/MnO₂ PHMs is 0.5, 1.1, 2.1, and 3.26 log, respectively. Even under the infrared irradiation above 830 nm with a light intensity of 206.2 mW/cm², 0.3%Ag/MnO₂ PHMs still achieves bacterial inactivation with a residual cell of 3.94

log₁₀ cfu/mL. These results suggest that 0.3%Ag/MnO₂ PHMs demonstrates UV-vis-NIR, vis-NIR, and NIR catalytic activity with high efficiency.

Due to the strong absorption of Ag/MnO₂ PHMs in the full solar spectrum region (Fig. 3c), there are two possible mechanisms that may contribute to its highly efficient solar light driven *E. coli* inactivation, (1) photocatalysis: electron and hole can be separated by the absorption of photons with energy higher than the band gap of the semiconductor, inducing the redox reaction of the reactive species [52]; (2) thermocatalysis: the surface temperature of the catalyst can be enhanced by the absorption of photons due to photothermal conversion, thus stimulating the thermocatalysis and may also trigger surface reactive species [53]. To clarify this issue, the photocatalytic inactivation of

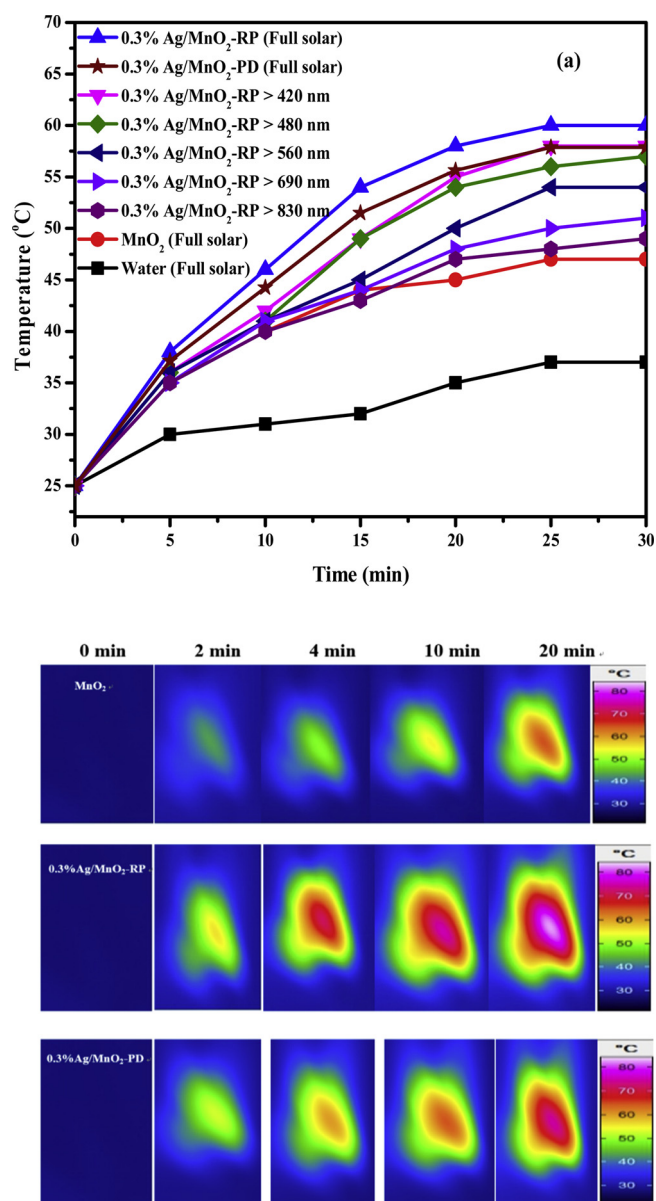


Fig. 5. (a) Temperature versus time plots recorded in water, MnO₂ and 0.3%Ag/MnO₂ PHMs suspension upon irradiation by Xenon lamp (0.25 W cm^{-2}) with/without different filter (420 nm, 480 nm, 560 nm, 690 nm and 830 nm); and (b) Thermo images for MnO₂ and 0.3%Ag/MnO₂ PHMs.

0.3%Ag/MnO₂ PHMs with full solar spectrum irradiation at room temperature was conducted. In this case, about $3.42 \log_{10} \text{ cfu/mL}$ cell inactivation was detected (Fig. 4c), indicating that 0.3%Ag/MnO₂ PHMs has some photocatalytic activity based on the conventional photocatalysis mechanism. However, no detectable *E. coli* loss was obtained for MnO₂ PHMs at room temperature under the irradiation by the Xenon lamp, suggesting that limited photocatalytic activity of MnO₂ PHMs. Obviously, the deposited atomic Ag even with 0.1% can efficiently enhance the photocatalytic inactivation of *E. coli*, mainly caused by the narrowed bandgap of MnO₂ after Ag doping. This means that the highly efficient bacterial inactivation may also originate from the solar light-driven thermocatalysis, i.e. Ag/MnO₂ absorb the solar energy, and transform the absorbed solar energy to thermal energy, leading to an increase in the temperature and form reactive species of the Ag/MnO₂ suspension.

To identify the solar light driven thermocatalysis, the photothermal conversion ability of the catalysts was studied firstly. The solution

temperature evolution of the catalysts with the irradiation of Xenon lamp under the conditions identical to the photocatalytic test was measured. As shown in Fig. 5a, the full solar spectrum irradiation leads to a rapid increase in the temperature of MnO₂ PHMs solution to an equilibrium temperature (T_{eq}) of 46 °C at which the equilibrium between the absorption of photon energy by MnO₂ PHMs and the dissipation of energy to the surroundings is established. The temperature increase upon solar-light irradiation can thus be attributed to the heating effect of the energy released by the quick non-radiative recombination of the electron-hole pairs produced by the d-d transitions of Mn ions in MnO₂ PHMs upon the absorption of photons [54]. In contrast, the T_{eq} of 0.3% Ag/MnO₂ PHMs (61 °C) is much higher than that of MnO₂ PHMs, indicating that the strong surface plasmonic absorption of Ag nanoparticles in Ag/MnO₂ PHMs makes a considerable contribution to the surface temperature increase. Besides the local heating effect of atomic Ag, its excellent thermal conductivity and low heat capacity also can accelerate the rise of temperature through the heat diffusion from MnO₂ to Ag [18]. Moreover, the T_{eq} of 0.3%Ag/MnO₂ with visible-infrared or infrared irradiation above 420, 480, 560, 690, and 830 nm were also measured; the corresponding T_{eq} is 58, 57, 54, 51, and 49 °C, respectively (Fig. 5a). It should be noted that pure water displays a limited enhancement in temperature (35 °C) under the same irradiation conditions, which is attributed to the heating effect from the infrared irradiation with the Xenon lamp. Therefore, the results indicate atomic Ag doping can enhance the photothermal conversion of MnO₂, and it can proceed with full solar, visible-infrared and even infrared light. Moreover, as shown in Fig. 5a, the T_{eq} of both 0.3%Ag/MnO₂-PR (61 °C) is much higher than that of 0.3%Ag/MnO₂-PD (50 °C) MnO₂ PHMs, indicating the high dispersion of atomic Ag is beneficial for the temperature increasing. Furthermore, the further experiments of individual Ag catalysis were carried out with the irradiation of Xenon lamp under the same conditions, the solution temperature evolution was tested, and the result was showed in Fig. S4. Compared with water solution only (37 °C), the solution temperature was merely promoted with 0.03 mg Ag (37.5 °C) and 3 mg Ag (41 °C). Therefore, the individual Ag also has some contribution to the whole photothermocatalytic reaction.

Additionally, to directly investigate the surface photothermal effect for 0.3%Ag/MnO₂ PHMs in converting light into heat, the IR thermocamera was also utilized. As shown in Fig. 5b, the color of images was varied with the degree of temperature and the right scale is corresponding to different color. As shown in Fig. 5b, With the increase of irradiation time, the color of 0.3%Ag/MnO₂ PHMs-RP images became brighter and temperature rose significantly to over 80 °C, while lower temperature increased for the 0.3%Ag/MnO₂ PHMs-PD (near 80 °C) and the MnO₂ PHMs (70 °C), further confirming the increment of thermal energy was mainly attributed to its highly dispersed atomic Ag rather than the elemental Ag cluster.

Furthermore, to study the contribution of thermocatalysis for *E. coli* inactivation, the inactivation efficiency of 0.3% Ag/MnO₂ PHMs suspension at the different controlled temperature in dark was also measured. As shown in Fig. 4c, the thermocatalysis activity of pure MnO₂ PHMs is very low, as no significant cells' loss can be observed even increasing the solution temperature from 40 to 60 °C within 10 min reaction. In contrast, loading Ag on MnO₂ leads to a considerable improvement in thermocatalytic activity. When the reaction temperature increases above 40 °C, *E. coli* starts to be inactivated. Further increase the temperature to 60 °C, almost $1.85 \log_{10} \text{ cfu/mL}$ of cells loss was achieved. This result indicates thermocatalytic *E. coli* inactivation can proceed for 0.3%Ag/MnO₂ PHMs and atomic Ag doping can enhance the thermocatalytic ability of MnO₂ PHMs. The atomic Ag can induce higher reducibility for MnO₂ (Fig. 1b), it results in much higher activity of lattice oxygen in MnO₂, thus promoting the thermocatalysis to inactivate *E. coli* under higher temperature.

Do the photocatalysis and the solar light driven thermocatalysis on the 0.3%Ag/MnO₂ PHMs occur independently for *E. coli* inactivation?

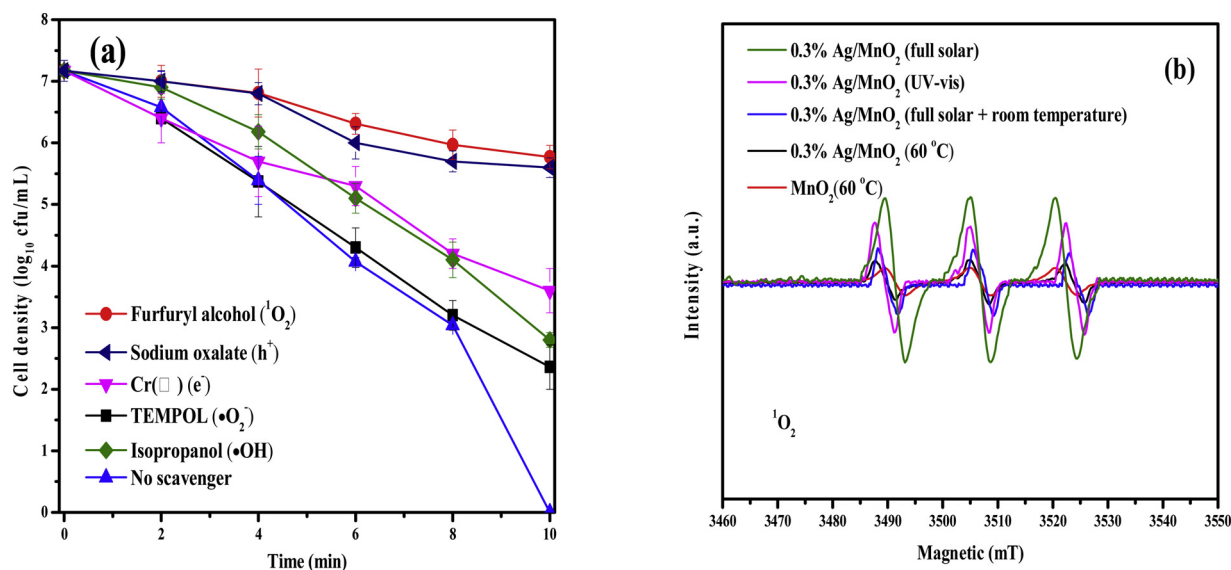


Fig. 6. (a) Inactivation efficiency against *E. coli* (10⁷ cfu/mL) by 0.3%Ag/MnO₂ PHMs with different scavengers (0.5 mM Cr(VI), 1 mM isopropanol, 1 mM TEMPOL, 1 mM FFA, and 1 mM sodium oxalate, respectively); (b) ESR spectra of ¹O₂ generated by 0.3%Ag/MnO₂ PHMs under full solar spectrum and UV-vis irradiation, as well as under dark condition, respectively.

To clarify this issue, the comparison in the *E. coli* inactivation efficiency was depicted in Fig. 4d. It can be found that the *E. coli* inactivation efficiency under full solar light (7.11 log₁₀ cfu/mL of cell loss) is much higher than the corresponding summation of the photocatalysis (2.67 log₁₀ cfu/mL of cell loss, room temperature) and the thermocatalysis even at the reaction temperature of 60 °C in dark (1.85 log₁₀ cfu/mL of cells loss). This result clearly indicates the existence of a synergetic effect of the photocatalysis and thermocatalysis on the 0.3%Ag/MnO₂ PHMs under the full solar spectrum irradiation. Similarly, the synergistic effect of thermocatalysis (0.52 log₁₀ cfu/mL) and photocatalysis (0.28 log₁₀ cfu/mL) was also observed for MnO₂ PHMs with 1.5 log₁₀ cfu/mL cells' loss under solar light irradiation. Obviously, the much higher photocatalytic activity and more efficient thermocatalysis of 0.3%Ag/MnO₂ PHMs results in its much higher photothermocatalytic activity than MnO₂ PHMs under the full solar irradiation.

Because MnO₂ only exhibits limited photocatalytic bactericidal activity (0.52 log₁₀ cfu/mL for photothermocatalysis; 0.28 log₁₀ cfu/mL for photocatalysis), the contribution from modified Ag, Mn³⁺, oxygen vacancies or the silver itself were further analyzed. In contrast, through using the performance of 0.3%Ag/MnO₂ PHMs to subtract the performance of MnO₂ PHMs, the deduced photothermocatalytic and photocatalytic inactivation efficiency by the modified 0.3%Ag is 1.85 log₁₀ cfu/mL and 2.39 log₁₀ cfu/mL (Fig. 4d).

About the role of Mn³⁺, tetrasodium pyrophosphate (Na₄P₂O₇), a widely-used scavenger was added to complex Mn³⁺ [55–57]. As shown in Fig. 4e, the inactivation efficiency of 0.3%Ag/MnO₂ is inhibited to some content (4.8 log₁₀ cfu/mL for photothermocatalysis; 0.6 log₁₀ cfu/mL for photocatalysis). The deduced photothermocatalytic and photocatalytic inactivation of *E. coli* by Mn³⁺ is 2.3 log₁₀ cfu/mL and 1.085 log₁₀ cfu/mL, which clearly confirms the photothermocatalytic and photocatalytic role of Mn³⁺.

About the role of oxygen vacancies, the pre-oxidized 0.3%Ag/MnO₂ sample was used (0.3%Ag/MnO₂ was previously oxidized by O₃ for 30 min, thus the oxygen vacancy was replenished by O element). References have been reported that the oxidation reaction with O₃ can fill up the oxygen vacancies [58,59]. Moreover, the Raman results (Fig. 3a) also confirmed lower oxygen vacancies in the pre-oxidized 0.3%Ag/MnO₂ PHMs, since the I_D/I_G value (3.006%) of pre-oxidized 0.3%Ag/MnO₂ PHMs was lower than that of fresh 0.3%Ag/MnO₂ PHMs (4.89%), respectively. As shown in Fig. 4e, the inactivation efficiency of

pre-oxidized 0.3%Ag/MnO₂ PHMs (5.71 log₁₀ cfu/mL for photothermocatalysis; 1.73 log₁₀ cfu/mL for photocatalysis) was greatly inhibited. The result clearly confirmed the photothermocatalytic and photocatalytic bactericidal role of oxygen vacancy, as the deduced photothermocatalytic and photocatalytic inactivation of *E. coli* by oxygen vacancy is 1.4 log₁₀ cfu/mL and 0.94 log₁₀ cfu/mL.

In comparison, the photothermocatalytic and photocatalytic bactericidal role is in the rank of modified atomic Ag (5.61 log₁₀ cfu/mL, 2.39 log₁₀ cfu/mL) > Mn³⁺ (2.3 log₁₀ cfu/mL, 1.085 log₁₀ cfu/mL) > oxygen vacancy (1.4 log₁₀ cfu/mL, 0.94 log₁₀ cfu/mL) > MnO₂ (1.5 log₁₀ cfu/mL, 0.28 log₁₀ cfu/mL) > elemental Ag (0.34 log₁₀ cfu/mL). The results clearly confirmed the critical role of atomic Ag to the enhanced photothermocatalytic and photocatalytic activity of MnO₂ PHMs.

To further investigate the inactivation capability of 0.3%Ag/MnO₂ PHMs under simulated authentic water conditions, different initial pH and cell density experiments were also performed. As shown in Fig. S2a, 0.3%Ag/MnO₂ PHMs exhibited wide-pH suitability and only slightly higher efficiency was observed at pH 9.29 than 5.60, 7.32. The better inactivation under alkaline condition is mainly due to the more easy generation of reactive species like [•]OH generation [7]. As depicted in Fig. S2b, with the increase of initial cell density from 3 log₁₀ cfu/mL to 9 log₁₀ cfu/mL, 0.3%Ag/MnO₂ PHMs also can maintain good inactivation capability with the prolonged irradiation time from 2 min to 14 min.

When illuminated with solar light, the photothermal conversion of Ag/MnO₂ PHMs gives rise to the rapid increase in the temperature of supported Ag, which may trigger the fast release of Ag⁺ [18]. To identify this, the released amount of Ag⁺ was measured (Fig. S3). However, only limited Ag⁺ (ca. 4.2 ppb) can be determined and no cell loss with the addition of 5 µg/L of Ag⁺ in the control experiment, indicating the antibacterial activity was attributed to the photothermocatalytic effect of 0.3%Ag/MnO₂ rather than the released Ag⁺. In contrast, over 26 ppb µg/L of Ag⁺ ions were released by 0.3%Ag/MnO₂-PD. This also confirms the good stability of atomic Ag/MnO₂ PHMs prepared by redox-preparation.

3.3. Role of various reactive species

The efficient photothermal conversion generated heat by Ag/MnO₂ PHMs can trigger the thermocatalysis to inactivate *E. coli*; it may also

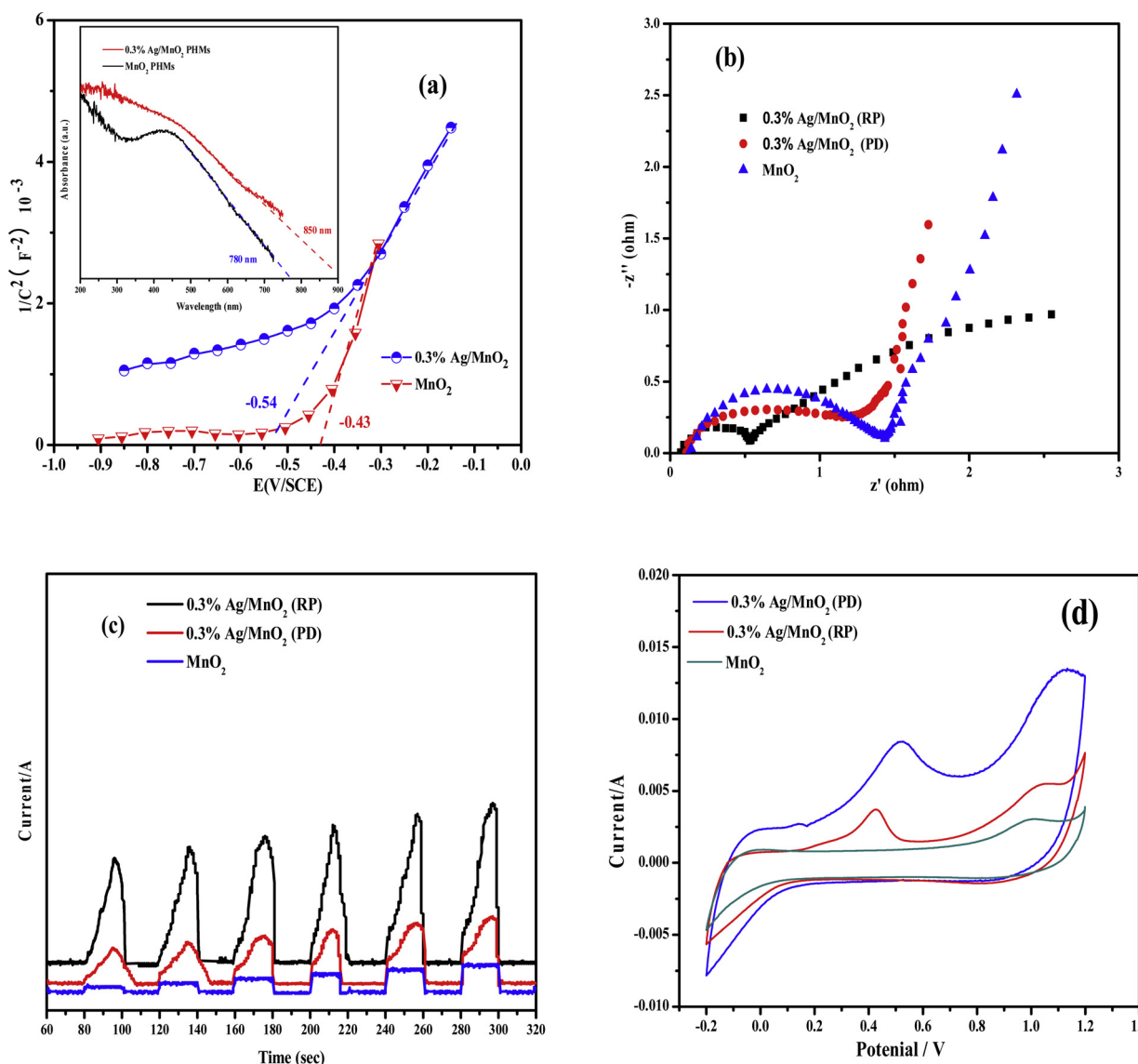


Fig. 7. (a) Mott-Schottky plots (inset of UV-vis-NIR DRS spectra), (b) Electrochemical impedance spectroscopy (EIS) spectra, (c) Time-based photocurrent response and (d) Cyclic voltammetry (CV) curves of MnO₂ and 0.3%Ag/MnO₂ PHMs.

enhance the photocatalysis to form more free radicals to attack *E. coli*. Trapping experiments were first used to evaluate the role of generated reactive species during the reaction by adding specific chemical scavengers, including Cr(VI) (e^-), sodium oxalate (h^+), isopropanol ($\cdot OH$), furfuryl alcohol (1O_2) and TEMPOL ($\cdot O_2^-$) [7,8,14]. As shown in Fig. 6a, compared with that of no scavenger, the *E. coli* inactivation efficiency of 0.3% Ag/MnO₂ PHMs exhibited obviously decrease after the addition of sodium oxalate, indicating the major bactericidal role of h^+ . In contrast, the addition of Cr(VI) to trap e^- also shows some effect on the disinfection, suggesting the moderate bactericidal role of e^- . Besides, some inhibited antibacterial activity also occurs in the presence of TEMPOL and isopropanol, suggesting the limited antibacterial role of $\cdot O_2^-$ and $\cdot OH$ species. Actually, based on the Schottky curve in Fig. 7a, it is reasonable to propose that the electrons in the CB of 0.3% Ag/MnO₂ PHMs can reduce the absorbed oxygen to generate $\cdot O_2^-$ ($E_0(O_2/\cdot O_2^-) = -0.33$ eV vs NHE)) and H₂O₂, which subsequently undergo facile disproportionation to produce $\cdot OH$ [7,8]. Moreover, plasmonic electrons generated by exciting the Ag NPs also can inject into the CB of MnO₂, reducing the surface oxygen to forming $\cdot O_2^-$ and $\cdot OH$ radicals via chain reactions [14]. Importantly, the inactivation of *E. coli* was almost totally inhibited by adding furfuryl alcohol (1O_2 , FFA,

$k = 1.2 \times 10^8$ M⁻¹ s⁻¹), suggesting 1O_2 was the critical reactive species in the reaction [7]. As shown in Fig. 6b, it is worth noting that the signal of DMPO degradation with 1:1:1 characteristic intensity has been observed for the 0.3% Ag/MnO₂ PHMs under Xenon lamp irradiation, which is ascribed to the production of 1O_2 [7]. Especially, the intensity of 1O_2 signal from full solar light was stronger than that of room temperature and UV-vis alone, indicative of the enhanced generation of reactive species by the photothermal effect. Notably, under dark condition, both 0.3% Ag/MnO₂ PHMs and MnO₂ PHMs can generate 1O_2 at 60 °C, suggesting the heat can trigger thermocatalysis to generate reactive oxygen species for the observed cell inactivation in Fig. 4c. The much higher intensity of 1O_2 under full light irradiation than that of room temperature with full light irradiation or dark condition, further confirming the synergism of photocatalysis and thermocatalysis in 0.3%Ag/MnO₂ PHMs. As identified above, 1O_2 and h^+ were the major reactive species and responsible for the inactivation of *E. coli*.

3.4. Mechanism of enhanced solar light driven *E. coli* inactivation

Based on the considerable enhancement of *E. coli* inactivation performance by Ag/MnO₂ PHMs, it is reasonable to conclude the critical

role of atomic Ag. The Mott-Schottky (MS) plots were first utilized to analyze the effect of single-atom Ag doping to MnO_2 . As shown in Fig. 7a, the flat band potential of MnO_2 and 0.3%Ag/ MnO_2 PHMs is -0.54 V and -0.43 V, respectively, which is close to the conduction band (CB) edge [14]. Based on the calculated band gap (1.55 and 1.46 V, inset of Fig. 7a), the valence band (VB) of MnO_2 and 0.3%Ag/ MnO_2 PHMs could be estimated to be 1.01 and 1.03 V, respectively. This result indicated that atomic Ag doping can narrow the band gap of MnO_2 , beneficial for the electron-hole separation in 0.3%Ag/ MnO_2 PHMs. Moreover, electrochemical tests were applied to further identify the accelerated migration and interface reaction ability of the charges in catalysts [60,61]. Generally, a smaller arc size in electrochemical impedance spectra (EIS) reflects lower charge transfer resistance on the electrode surface [62]. As shown in Fig. 7b, a smaller arc radius was observed for 0.3%Ag/ MnO_2 PHMs than that of MnO_2 PHMs, indicating the separation and transfer efficiency of photogenerated e^- - h^+ was greatly enhanced through the Ag- MnO_2 interface. In addition, the photocurrent response of the 0.3%Ag/ MnO_2 PHMs was also significantly increased and maintained with several on-off cycles in comparison to MnO_2 PHMs (Fig. 7c), further confirming that the atomic Ag doping owns a fast and stable interfacial charge transfer [62]. Moreover, as shown in Fig. 7c, photocurrent response of 0.3%Ag/ MnO_2 PHMs exhibited slightly temperature-improved within 5 min. This increase in photocurrent is consistent with the increase of the electron lifetime [63], further confirming that the temperature increase accelerates charge transfer.

Similar phenomena was also observed in the CV curves of Fig. 7d, the current of Ag/ MnO_2 PHMs are much higher than that of MnO_2 PHMs, verifying the presence of higher surface charge transfer on Ag/ MnO_2 PHMs [62]. It should be noted that the contact of atomic Ag nanoparticles on MnO_2 PHMs greatly determine the photothermocatalytic activity with the reason that the close contact is the key to achieving efficient charge transfer. As identified by Fig. 7b–d, the electron transfer efficiency from MnO_2 to Ag cluster (Ag/ MnO_2 PHMs-PD) is much lower in comparison with that from MnO_2 to atomic Ag (Ag/ MnO_2 PHMs-RP). It is reasonable to propose that the interfacial contact area in 0.3%Ag/ MnO_2 PHMs-RP is much higher than that of 0.3%Ag/ MnO_2 PHMs-PD, which leads to the efficient charge transfer through maximum utilization of Ag NPs due to its higher dispersion of atomic Ag.

Upon solar light irradiation, the hot electrons in MnO_2 with narrowed band gap can be quickly separated and transferred by highly conductive Ag in realizing the spatial separation of hot electrons and holes. Meanwhile, higher concentrations of lower valent Mn and oxygen vacancies in 0.3% Ag/ MnO_2 PHMs (XPS and Raman results in Fig. 3) could also accelerate the separation of electron-hole pairs through providing active sites for surface O_L to capture electron [63]. Additionally, atomic Ag itself can also generate hot electrons by its plasmonic effect, collectively work with the hot electrons transfer on the Ag- MnO_2 interface to participate in the formation of reactive species and achieve the enhanced photocatalysis for Ag/ MnO_2 PHMs. Theoretically, the photogenerated e^- from CB of 0.3%Ag/ MnO_2 PHMs is negative enough to reduce $\text{O}_2/\text{H}_2\text{O}$ into $^1\text{O}_2$ (-0.11 V, [7]), resulting in the critical role of $^1\text{O}_2$ in Fig. 6a. However, the photogenerated h^+

from VB of 0.3%Ag/ MnO_2 PHMs is not positive enough to oxidize $\text{O}_2/\text{H}_2\text{O}$ into $^{\cdot}\text{OH}$ (2.8 V, [14]), causing the limited bactericidal role of $^{\cdot}\text{OH}$. Instead, the h^+ is still powerful to directly attack *E. coli*, consistent with the results in Fig. 6a.

Simultaneously, the solar light-driven thermocatalysis also occurs on the Ag/ MnO_2 PHMs. It is well known that the thermocatalytic oxidation on MnO_2 proceeds via the Mars-van Krevelen mechanism: molecules adsorbed on the surface of MnO_2 are oxidized by its surface O_L , and the produced oxygen vacancies are subsequently replenished by gas-phase O_2 [64]. The reducibility of the surface O_L in MnO_2 thus plays a decisive role in its thermocatalytic activity because the reduction of MnO_2 is more sluggish than the re-oxidation of reduced MnO_2 [65]. H_2 -TPR in Fig. 3c has confirmed the higher reducibility of MnO_2 PHMs after atomic Ag doping, which means that the O_L of Ag/ MnO_2 PHMs is in a higher activity for thermocatalysis. Moreover, the more efficient photothermal conversion for Ag/ MnO_2 than MnO_2 PHMs was identified in Fig. 5a. The reason is that atomic Ag is with broad absorption bands spanning the UV–vis–NIR wavelengths, which can induce multiple scattering events and increase photon absorption probability, resulting in localized intense heating on MnO_2 . Also, atomic Ag itself with high thermal conductivity and low heat capacity also can accelerate the rise of temperature through the heat diffusion from MnO_2 to Ag. Therefore, the more efficient photothermal conversion of Ag/ MnO_2 than MnO_2 PHMs together with its higher thermocatalytic activity result in its much higher *E. coli* inactivation efficiency.

To put more insight in the synergetic effect of photothermocatalysis, the effect of the solar light irradiation on the reducibility of 0.3% Ag/ MnO_2 PHMs was investigated by H_2 -TPR in dark and with the irradiation of the Xenon lamp. As shown in Fig. 3b, notably, compared to H_2 -TPR in dark, the full solar spectrum irradiation of Xenon lamp leads to a considerable shift of H_2 consumption peak to lower temperature, indicative of higher activity of O_L in Ag/ MnO_2 PHMs. This may arise from the following reason: the photogenerated holes in MnO_2 upon full solar irradiation leads to the formation of O^- species from O_L ($h^+ + \text{O}_L^{2-} = \text{O}^-$) and activate O_L simultaneously, and the active O^- species may react with H_2 to cause the H_2 consumption peak shift to lower temperature [66]. Moreover, irradiation with the full solar spectrum resulted in a significant increase in the total H_2 consumption amount (Table 3), suggesting that more active O_L was produced upon solar light irradiation. Therefore, the highly efficient photothermocatalysis is considerably promoted by the synergetic effect through O_L , the hot h^+ generated by photocatalysis can promote the activity and amount of O_L , thus considerably improving the thermocatalysis activity of 0.3%Ag/ MnO_2 PHMs. Consistently, the consumption of O_L was observed in the used 0.3%Ag/ MnO_2 PHMs in Fig. 1c and Table 2.

As shown in Scheme 2, with the solar light irradiation of Ag/ MnO_2 PHMs, the MnO_2 PHMs not only generate heat through photothermal effect, but also produce hot charge carriers. Both heat and hot electrons then transfer to atomic Ag through Ag- MnO_2 interface, resulting in the elevated temperature as well as separation of electrons and holes to attack cell by heat and reactive species. Meanwhile, the plasmonic Ag itself exhibits strong local heating effect and generate hot electrons in the entire solar irradiation, which also help to kill bacteria by heat and reactive species. Especially, the 3D porous hollow structure of MnO_2

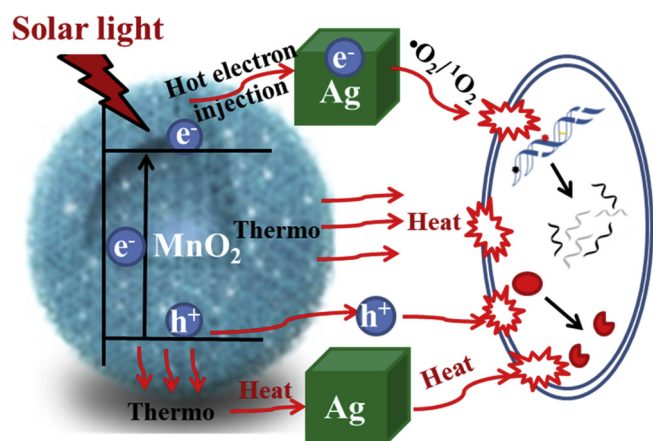
Table 3

Reduction temperature and H_2 consumption of MnO_2 and Ag/ MnO_2 PHMs.

Catalysts	Reduction temperatures ($^{\circ}\text{C}$) ^a			H_2 consumptions (mmol/g) ^b		
	peak 1	peak 2	peak 3	peak 1	peak 2	peak 3
MnO_2	200	307	492	0.79	0.68	3.34
0.3%Ag/ MnO_2	114	154	250	1.04	2.83	3.88
0.3%Ag/ MnO_2 (irradiation)	85	124	205	1.19	3.12	4.29

^a Reduction temperatures corresponding to the maximum values of reduction peaks in the H_2 -TPR result.

^b H_2 consumptions calculated by reduction peak areas.



Scheme 2. Mechanism of *E. coli* inactivation with Ag/MnO₂ PHMs under solar light irradiation.

may provide large active sites and promote the mass transfer process to facilitate the reaction [22,23].

3.5. The bacterial damage process

The morphology of *E. coli* at different stages of the disinfection process was imaged by SEM in Fig. 8a–c. The rod-shaped morphology (Fig. 8a) of *E. coli* cells in the beginning became deformed with some bulges and pits on the surfaces, seriously distorted and fractured with prolong treated (Fig. 8b), indicating that generated reactive species and heat efficiently attack and destroy the cells' envelope. The *E. coli* cells were completely deformed after 10 min treated. Similarly, fluorescence tests were also indicated the damage of *E. coli* cells by 0.3%Ag/MnO₂ PHMs. Green fluorescent stain for both live and dead bacteria, and red fluorescent stain for cells with compromised cellular membranes. The cells red fluorescence increased and nearly completely to replace green

fluorescence in number within 10 min treated, as shown in Fig. 8e and f, indicating that *E. coli* cells were sustainably destructed and debris were adsorbed on the surfaces of 0.3%Ag/MnO₂ PHMs [7,14].

The oxidative stress mediated by 0.3%Ag/MnO₂ PHMs was examined using glutathione oxidation assay. Glutathione (GSH) is a tripeptide with a thiol group, serves as one of the major cellular antioxidant enzymes in bacteria, with concentration ranging between 0.1 and 10 mM [67]. As an indicator of the oxidative stress induced by different nanomaterials, thiol groups (–SH) of glutathione can be oxidized to glutathione (GSH). GSH is involved in the intracellular oxidative balance and protects the cells against external electrophilic compounds, thereby the *E. coli* to quickly synthesize more GSH (from 1.5 to 2.05 $\mu\text{mol/L}$) to fight against the oxidation and heat attack in the first 5 min treatment (Fig. 9a). However, with prolonged treatment, GSH content in the cells sharply decreased from 2.05 to 0 $\mu\text{mol/L}$ within 30 min treated, indicating the fierce attack from Ag/MnO₂ PHMs exceeded the self-defense capability of *E. coli*.

Even if the cells have been inactivated, some injured cells in the initial phase still can self-repair their respiratory ability and then supply enough energy for regrowth after culture in nutrients [14]. As the key material for storing both vital and direct energy, the synthesis of ATP is directly responsible for cellular metabolic activity [32]. Therefore, ATPase (the ATP synthesis enzyme) was monitored to identify damaged metabolism, whose activity is in proportion to the elevated absorption intensity [64]. As shown in Fig. 9b, accumulated ATP content in the cells decreased with prolong treated (the amount of ATP at an incubation time of 60 min): initial cells contained almost 1.2×10^{-10} mmol ATP/cell, which then decreased to 3×10^{-11} mmol ATP/cell, and almost no ATP remained after 30 min treated, indicating the cells almost lost all the ability to synthesize ATP after a prolonged treatment period.

Notably, cell still can self-repair and regrow even when their proteins are damaged [64,65]. Only severe damage to the DNA can cause fatal, death of the cells. The leakage and decomposition of genomic DNA could be observed in Fig. 9c–e, which displays that the intensity of

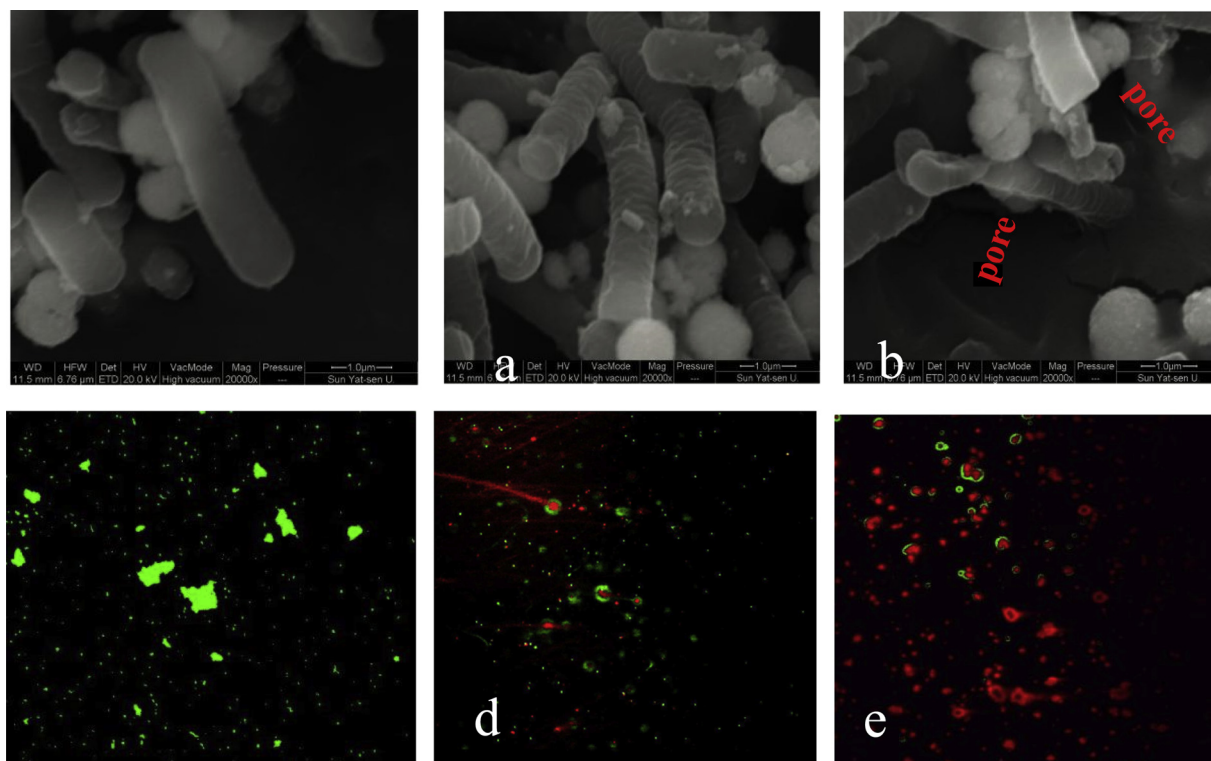


Fig. 8. SEM images and fluorescence microscopic images of *E. coli* (10^8 cfu/mL) treated by 0.3%Ag/MnO₂ PHMs with (a) 0 min, (b) 5 min, (c) 10 min under a Xenon lamp.

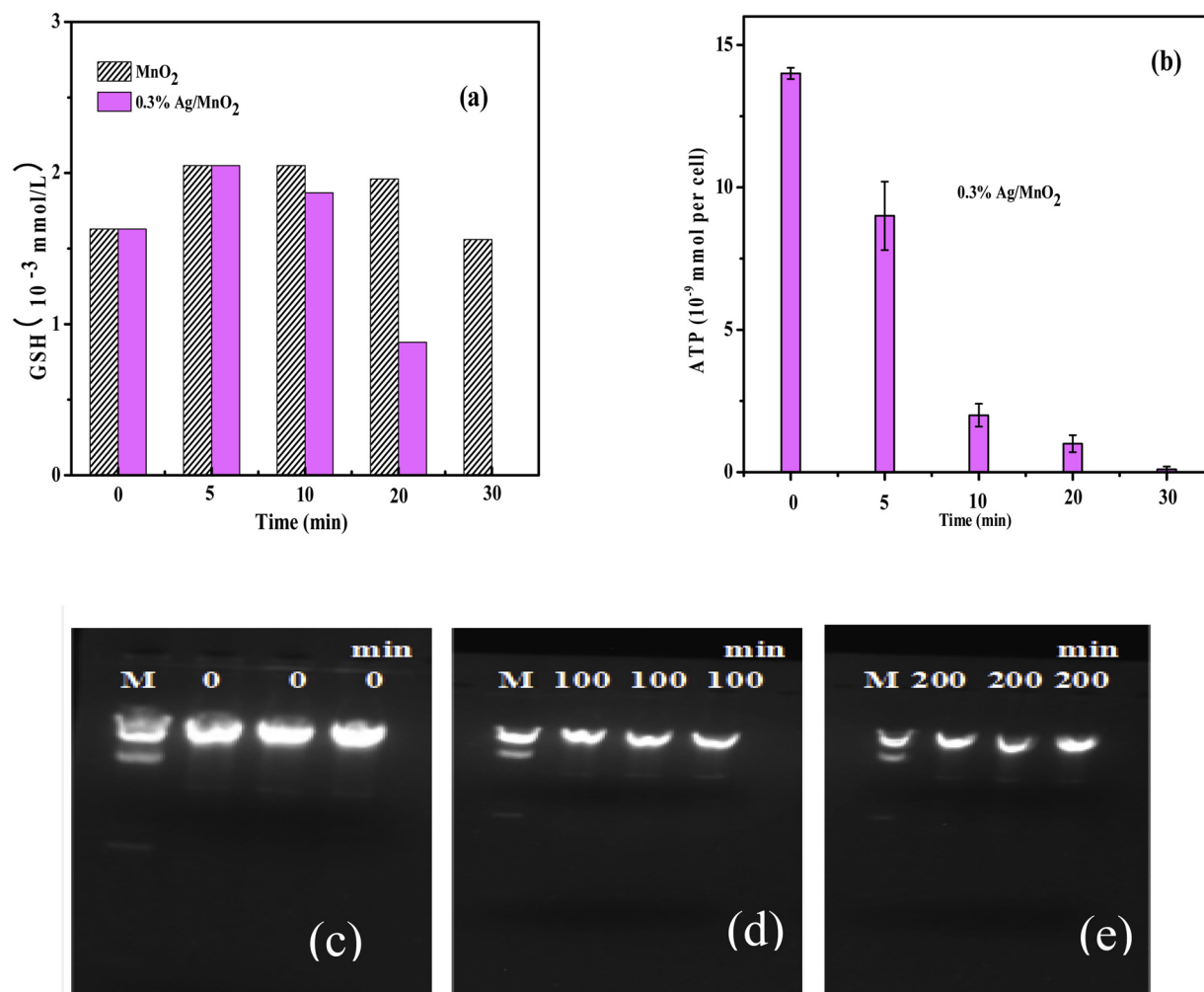


Fig. 9. The *E. coli* (10^7 cfu/mL) generation potential of GSH (a) and ATP (b) after photothermocatalytic inactivation for 0, 5, 10, 20 and 30 min, and (c–e) the leakage bacterial genomic DNA extracted from harvested cells (10^8 cfu/mL) during photocatalytic inactivation by 0.3%Ag/MnO₂ PHMs with (c) 0 min, (d) 100 min, (e) 200 min.

DNA bands decreased significantly within the 200 min of the process.

Within the test time-period, the incomplete elimination of the DNA bands means the total mineralization of *E. coli* by Ag/MnO₂ PHMs has not finished. Although the cell envelope and functional enzymes have been destructed mostly within the test-period, its residual organic fragment will compete with the DNA to consume the ROS and heat. Therefore, it still needs a longer reaction time to totally mineralize the biomolecules and even DNA [16]. In addition, during the bacterial inactivation process, the bacteria division and then the leakage of DNA from the cell were in a dynamic equilibrium, which also hinder the complete destruction of intracellular DNA.

4. Conclusions

In this work, the high dispersion of atomic Ag nanoparticles on MnO₂ porous hollow microspheres (the optimum 0.3%Ag/MnO₂ PHMs) was prepared by redox-precipitation methods, which achieved highly photothermocatalytic bacterial inactivation under solar light irradiation. Firstly, attributed to the high conductivity of Ag and its induced low valent Mn and oxygen vacancy, the excitation of MnO₂ by solar light produces hot charge carriers and then quickly transfers to Ag nanoparticles through Ag-MnO₂ interface, transforming into reactive species for photocatalysis. Secondly, the confined atomic Ag exhibits strong local heating effect and induces higher reducibility for MnO₂, considerably enhances the photothermal conversion and lattice oxygen

activity of MnO₂, thus promoting the thermocatalysis. Due to the synergistic effect of photocatalysis and thermocatalysis participating in photothermocatalytic reaction, thus the designed 3D Ag/MnO₂ PHMs exhibit superior inactivation efficiency towards *E. coli* under solar light.

Acknowledgments

The authors wish to thank the National Natural Science Foundation of China (Nos. 51578556, 21876212, 41603097, 41573086), Natural Science Foundation of Guangdong Province (Nos. 2015A030308005, S2013010012927, S2011010003416), Science and Technology Research Programs of Guangdong Province (No. 2014A020216009), and the Fundamental Research Funds for the Central Universities (No. 13lgjc10) for financially supporting this work. Dr. Xia was also supported by the Start-up Funds for High-Level Talents of Sun Yat-sen University (38000-18821111).

Appendix A. Supplementary data

Supplementary material related to this article can be found, in the online version, at doi:<https://doi.org/10.1016/j.apcatb.2018.12.056>.

References

- [1] M.A. Shannon, P.W. Bohn, M. Elimelech, J.G. Georgiadis, B.J. Marinas, A.M. Mayes,

- Science and technology for water purification in the coming decades, *Nature* 452 (2008) 301–310.
- [2] A. Epstein, B. Pokroy, A. Seminara, J. Aizenberg, *Proc. Natl. Acad. Sci. U. S. A.* 108 (2011) 995–1000.
 - [3] S. Ma, S. Zhan, Y. Jia, Q. Zhou, *ACS Appl. Mater. Interfaces* 7 (2015) 10576–10586.
 - [4] X. Yang, J. Qin, Y. Jiang, K. Chen, X. Yan, D. Zhang, *Appl. Catal. B: Environ* 166–167 (2015) 231–240.
 - [5] S. Loeb, R. Hofmann, J.H. Kim, *Environ. Sci. Technol. Lett.* 3 (2016) 73–80.
 - [6] S. Ma, S. Zhan, Y. Jia, Q. Zhou, *ACS Appl. Mater. Interfaces* 7 (2015) 21875–21883.
 - [7] D. Xia, H. He, H. Liu, Y. Wang, Q. Zhang, Y. Li, A. Lu, C. He, P.K. Wong, *Appl. Catal. B: Environ.* 238 (2018) 70–81.
 - [8] D. Xia, T. An, G. Li, W. Wang, H. Zhao, P.K. Wong, *Water Res.* 99 (2016) 149–161.
 - [9] P. Zhang, D. Wan, Z. Zhang, G. Wang, J. Hu, G. Shao, *Environ. Sci.-Nano* 5 (2018) 1813–1820.
 - [10] N. Lu, Z. Zhang, Y. Wang, B. Liu, L. Guo, L. Wang, J. Huang, K. Liu, B. Dong, *Appl. Catal. B: Environ.* 233 (2018) 19–25.
 - [11] J. Zhao, J. Nan, Z. Zhao, N. Li, J. Liu, F. Cui, *Appl. Catal. B: Environ.* 202 (2017) 509–517.
 - [12] B. Bai, J. Li, J. Hao, *Appl. Catal. B: Environ.* 164 (2015) 241–250.
 - [13] Q. Zhou, S. Ma, S. Zhan, *Appl. Catal. B: Environ.* 224 (2018) 27–37.
 - [14] D. Xia, Z. Shen, G. Huang, W. Wang, J. Yu, P.K. Wong, *Environ. Sci. Technol.* 49 (2015) 6264–6273.
 - [15] J. Fei, Y. Cui, X. Yan, W. Qi, Y. Yang, K. Wang, Q. He, J. Li, *Adv. Mater.* 20 (2008) 452–456.
 - [16] M. Mao, Y. Li, J. Hou, M. Zeng, X. Zhao, *Appl. Catal. B: Environ.* 174 (2015) 496–503.
 - [17] F. Cheng, Y. Su, J. Liang, Z. Tao, J. Chen, *Chem. Mater.* 22 (2010) 898–905.
 - [18] B. Bai, Q. Qiao, H. Arandiyán, J. Li, J. Hao, *Environ. Sci. Technol.* 50 (2016) 2635–2640.
 - [19] J. Jia, P. Zhang, L. Chen, *Appl. Catal. B: Environ.* 189 (2016) 210–218.
 - [20] M. Piumetti, D. Fino, N. Russo, *Appl. Catal. B: Environ.* 163 (2015) 277–287.
 - [21] X. Tan, Y. Wan, Y. Huang, C. He, Z. Zhang, Z. He, L. Hu, J. Zeng, D. Shu, *J. Hazard. Mater.* 321 (2017) 162–172.
 - [22] Z. He, D. Xia, Y. Huang, X. Tan, C. He, L. Hu, H. He, J. Zeng, W. Xu, D. Shu, *J. Hazard. Mater.* 344 (2018) 1198–1208.
 - [23] Q. Xu, W. Lei, X. Li, X. Qi, J. Yu, G. Liu, J. Wang, P. Zhang, *Environ. Sci. Technol.* 48 (2014) 9702–9708.
 - [24] B. Bai, Q. Qiao, H. Arandiyán, J. Li, J. Hao, *Environ. Sci. Technol.* 50 (2016) 2635–2640.
 - [25] X. Chen, S. Ku, Justin A. Weibel, E. Ximenes, X. Liu, M.R. Ladisch, S.V. Garimella, *ACS Appl. Mater. Inter.* 45 (2017) 39165–39173.
 - [26] Z. Zhang, X. Jiang, B. Liu, L. Guo, N. Lu, L. Wang, J. Huang, K. Liu, B. Dong, *Adv. Mater.* 30 (2018) 1705221.
 - [27] Z. Zhang, J. Huang, Y. Fang, M. Zhang, K. Liu, B. Dong, *Adv. Mater.* 29 (2017) 1606688.
 - [28] Z. Zhang, J. Huang, M. Zhang, Q. Yuan, B. Dong, *Appl. Catal. B: Environ.* 163 (2015) 298–305.
 - [29] J. Wu, Z. Zhang, B. Liu, Y. Fang, L. Wang, B. Dong, *Sol. RRL* 2 (2018) 1800039.
 - [30] Y. Zhu, Z. Zhang, N. Lu, R. Hua, B. Dong, *Chin. J. Catal.* (2019) 40, [https://doi.org/10.1016/S1872-2067\(18\)63182-1](https://doi.org/10.1016/S1872-2067(18)63182-1).
 - [31] S. Loeb, C. Li, J.-H. Kim, *Environ. Sci. Technol.* 1 (2018) 205–213.
 - [32] Y. Zhu, M. Ramasamy, D.K. Yi, *ACS Appl. Mater. Interfaces* 6 (2014) 15078–15085.
 - [33] Q. Yin, L. Tan, Q. Lang, X. Ke, L. Bai, K. Guo, R. Qiao, *Appl. Catal. B: Environ.* 224 (2018) 671–680.
 - [34] J. Jones, H. Xiong, A.T. Delariva, E.J. Peterson, H. Pham, S.R. Challa, G. Qi, S. Oh, M.H. Wiebenga, X.I. Pereira Hernández, Y. Wang, A.K. Datye, *Science* 353 (2016) 150–154.
 - [35] B. Qiao, A. Wang, X. Yang, L. Allard, Z. Jiang, Y. Cui, J. Liu, J. Li, T. Zhang, *Nat. Chem.* 3 (2011) 634–641.
 - [36] D. Xia, L. Hu, X. Tan, C. He, W. Pan, T. Yang, Y. Huang, D. Shu, *Appl. Catal. B: Environ.* 185 (2016) 295–306.
 - [37] J. Chen, D. Yan, Z. Xu, X. Chen, W. Xu, H. Jia, J. Chen, *Environ. Sci. Technol.* 52 (2018) 4728–4737.
 - [38] D. Xia, T. An, G. Li, Y. Li, H.Y. Yip, H. Zhao, P.K. Wong, *Water Res.* 99 (2016) 149–161.
 - [39] D. Xia, T.W. Ng, T. An, G. Li, Y. Li, H.Y. Yip, H. Zhao, A. Lu, P.K. Wong, *Environ. Sci. Technol.* 47 (2013) 11166–11173.
 - [40] Z. Qu, Y. Bu, Y. Qin, Y. Wang, Q. Fu, *Appl. Catal. B: Environ.* 132–133 (2013) 353–362.
 - [41] F. Wang, H. Dai, J. Deng, G. Bai, K. Ji, Y. Liu, *Environ. Sci. Technol.* 46 (2012) 4034–4041.
 - [42] Y. Yang, Y. Li, M. Zeng, M. Mao, L. Lan, H. Liu, J. Chen, X. Zhao, *Appl. Catal. B: Environ.* 224 (2018) 751–760.
 - [43] J. Wang, J. Li, C. Jiang, P. Zhou, P. Zhang, J. Yu, *Appl. Catal. B: Environ.* 204 (2017) 147–155.
 - [44] L. Lan, Y. Li, M. Zeng, M. Mao, L. Ren, Y. Yang, H. Liu, L. Yun, X. Zhao, *Appl. Catal. B: Environ.* 203 (2017) 494–504.
 - [45] S. Rong, P. Zhang, F. Liu, Y. Yang, *ACS Catal.* 8 (2018) 3435–3446.
 - [46] J. Hou, Y. Li, M. Mao, L. Ren, X. Zhao, *ACS Appl. Mater. Interfaces* 6 (2014) 14981–14987.
 - [47] F. Liu, M. Zeng, Y. Li, Y. Yang, M. Mao, X. Zhao, *Adv. Funct. Mater.* 26 (2016) 4518–4526.
 - [48] Y. Xia, H. Dai, L. Zhang, J. Deng, H. He, C. Au, *Appl. Catal. B: Environ.* 100 (2010) 229–237.
 - [49] H. Liu, Y. Li, Y. Yang, M. Mao, M. Zeng, L. Lan, L. Yun, X. Zhao, *J. Mater. Chem. A* 4 (2016) 9890–9899.
 - [50] J. Hou, Y. Li, M. Mao, Y. Yue, G. Greaves, X. Zhao, *Nanoscale* 7 (2015) 2633–2640.
 - [51] Z. Khan, P. Kumar, Kabir-ud-Din, *J. Colloid Interface Sci.* 290 (2005) 184–189.
 - [52] M. Altaf, M. Akram, Kabir-ud-Din, *Colloids Surfaces B* 73 (2009) 308–314.
 - [53] M. Akram, M. Altaf, Kabir-ud-Din, *Colloids Surfaces B* 82 (2011) 217–223.
 - [54] D. Xia, W. Xu, Y. Wang, J. Yang, Y. Huang, L. Hu, C. He, D. Shu, D.Y.C. Leung, Z. Pang, *Environ. Sci. Technol.* 52 (2018) 13399–13409.
 - [55] S. Afzal, X. Quan, J. Zhang, *Appl. Catal. B* 206 (2017) 692–703.
 - [56] Q. Zhou, S. Ma, S. Zhan, *Appl. Catal. B* 224 (2018) 27–37.
 - [57] Q. Yin, L. Tan, Q. Lang, X. Ke, L. Bai, K. Guo, R. Qiao, S. Bai, *Appl. Catal. B* 224 (2018) 671–680.
 - [58] L. Hu, H. He, D. Xia, Y. Huang, J. Xu, H. Li, C. He, W. Yang, D. Shu, P.K. Wong, *ACS Appl. Mater. Interf.* 10 (2018) 18693–18708.
 - [59] Q. Zhou, S. Ma, S. Zhan, *Appl. Catal. B: Environ.* 224 (2018) 27–37.
 - [60] J. Hou, L. Liu, Y. Li, M. Mao, H. Lv, X. Zhao, *Environ. Sci. Technol.* 47 (2013) 13730–13736.
 - [61] J. Hou, Y. Li, M. Mao, L. Ren, X. Zhao, *ACS Appl. Mater. Interfaces* 6 (2014) 14981–14987.
 - [62] T. Berger, M. Sterrer, O. Diwald, E. Knozinger, D. Panayotov, T.L. Thompson, J.T. Yates Jr., *J. Phys. Chem. B* 109 (2005) 6061–6068.
 - [63] K. Rasool, M. Helal, A. Ali, C.E. Ren, Y. Gogotsi, K.A. Mahmoud, *ACS Nano* 10 (2016) 3674–3684.
 - [64] M.-C. Wu, A.R. Deokar, J.-H. Liao, P.-Y. Shih, Y.-C. Ling, *ACS Nano* 10 (2013) 3674–3684.
 - [65] C. Soci, A. Zhang, B. Xiang, S.A. Dayeh, D.P.R. Aplin, J. Park, X.Y. Bao, Y.H. Lo, D. Wang, *Nano Lett.* 7 (2007) 1003–1009.